Mechanics of Bacterial Interaction and Death on Nanopatterned Surfaces

Amar Velic[a,b], Jafar Hasan[a,b], Zhiyong Li[a,b], Prasad K.D.V. Yarlagadda[a,b,*]

[a] School of Mechanical, Medical and Process Engineering, Queensland University of Technology, Brisbane, Queensland 4000, Australia
[b] Centre for Biomedical Technologies, Queensland University of Technology, Brisbane, Queensland 4000, Australia

* Prasad K.D.V. Yarlagadda, 2 George Street, Brisbane QLD 4000, Australia, +617 3138 5167

Email: y.prasad@qut.edu.au

0000-0002-5134-0502 (Amar Velic), 0000-0002-0956-6145 (Jafar Hasan), 0000-0002-6814-9165 (Zhiyong Li), Prasad K.D.V. Yarlagadda (0000-0002-7026-4795)

Abstract

Nanopatterned surfaces are believed to kill bacteria through physical deformation, a mechanism which has immense potential against biochemical resistance. Due to its elusive nature, this mechanism is mostly understood through biophysical modelling. Problematically, accurate descriptions of the contact mechanics and various boundary conditions involved in the bacteria-nanopattern interaction remain to be seen. This may underpin conflicting predictions, found throughout the literature, regarding two important aspects of the mechanism – that is, its critical action site and relationship with geometry. Herein, a robust computational analysis of bacteria-nanopattern interaction is performed using three-dimensional finite element modelling which incorporates relevant continuum mechanical properties, multilayered envelope structure and adhesion interaction conditions. The model is applied to more accurately study the elusory mechanism and its enhancement via nanopattern geometry. Additionally, micrographs of bacteria adhered on a nanopatterned cicada wing are examined to further inform and verify the major modelling predictions. Together, the results indicate that nanopatterned surfaces do not kill bacteria predominantly by rupture in between protruding pillars, as previously thought. Instead, non-developable deformation about pillar tips is more likely to create a critical site at the pillar apex, which delivers significant in-plane strains and may locally rupture and penetrate the cell. The computational analysis also demonstrates that envelope deformation is increased by adhesion to nanopatterns with smaller pillar radii and spacing. These results further progress understanding of the mechanism of nanopatterned surfaces and help guide their design for enhanced bactericidal efficiency.

Statement of Significance

Nanopatterned surfaces show immense potential, however, their mechanism has not yet been well resolved. The present work challenges the prevailing dogma that bacteria are killed in the region between pillars, which has been the dominant view on the mechanism since the discovery of antibacterial nanopatterned surfaces over half a decade ago. Instead, it is clearly demonstrated that critical envelope strains consistent with rupture readily occur at the pillar tips, which locally perturb and may penetrate the cell. In addition, recommendations are given on how to increase envelope strain and concomitant killing efficiency through geometric design, which remains poorly understood and is needed to optimise nanopatterned surfaces.

Main Text

Introduction

Bacteria have a well-demonstrated proficiency for outsmarting biochemical attacks. This is most apparent in the case of antibiotics, which have seen dwindling effectiveness due to a myriad of individual-level and biofilm-specific mechanisms such as production of hydrolysing enzymes, overexpression of efflux and formation of persister phenotypes (1). Similarly, evidence has emerged of alcohol-based disinfectants becoming increasingly ineffective against certain human pathogens with longstanding clinical presence (2). These trends have spurred interest in non-biochemical killing actions which can circumvent existing resistance mechanism and may be more robust to evolved resistance (3).

Nanopatterned surfaces seem to elicit such a killing action. This killing action, discovered on cicada wings (4), is believed to be predominantly physical as evidenced by its ability to span vast biological and chemical diversities. For instance, nanopatterned surfaces can inactivate a range of biologically diverse cells, including bacteria of both Gram types (5), superbugs (6), viruses (7) and, problematically, human cells (8). Also, the mechanism can be incorporated into a variety of chemically diverse, natural and synthetic materials such as insect cuticle (4, 9), polymer (10, 11), titanium (12, 13), stainless steel (14) aluminium (6, 7) and silicon wafer (15, 16). Common to all these observations is the inclusion of a non-planar topography composed of non-developable, nanoscale surface features. Accordingly, nanopatterned surfaces are believed to kill bacteria by adhesion to these protruding features which physically deform the cell envelope via contact, possibly to the point of rupture (4). Consistent with this mechanism, indications of envelope damage can be seen in post-mortem micrographs of nanopattern-treated bacteria, which often show turgor loss (deflation) and cytoplasm leakage (9, 10, 17). Also, as expected for such a mechanism, killing efficiency has been found to be mediated by

physical or mechanical parameters such as envelope stiffness (18, 19), envelope extensibility (20, 21), pattern geometry (10, 22) and adhesion strength (23, 24), adding further support.

Given that directly characterising the deformation is not possible, due to the size and dynamic nature of the interaction, present understanding of the mechanism is informed by biophysical modelling. Modelling is also best suited to elucidate nanopattern geometry for enhanced killing efficiency, which remains elusive to experimental investigation due to the difficulties of selective and systematic variation of diameter, spacing and height (10, 22, 25, 26). That being said, accurate biophysical analysis remains to be seen. Previous attempts to model the deformation have been marred by use of misrepresentative loads (26, 27), a priori shape assumptions (25), monolayer envelope models (18) and plane strain simplifications of a non-developable, three-dimensional problem (28). Whilst these points of difference may initially seem trivial, they have a direct bearing on the deformation mechanics, and therefore underpin predictions about the critical action site and geometry enhancement of the physical mechanism. This is quite evident, for example, with the popular biophysical model by Pogodin and others (18) whose predictions of envelope rupture between pillars seem to conflict with commonly seen pillar penetration (11, 28-31). This incompatibility reflects the challenge of mathematically analysing the bacteria-nanopattern problem, which requires careful consideration of contact mechanics and boundary conditions.

To address this, the present work analyses the mechanics of adhesion-driven envelope deformation by computational methods, namely three-dimensional finite element analysis using ABAQUS/Standard (Dassault Systèmes Simulia Corp., Johnston, RI). Going beyond previous efforts, realistic properties and multilayered structure are incorporated into a continuum model of a Gram-negative envelope which is brought into contact with a nanopattern using loads and boundary conditions that mimic adhesion. The model is used to study the magnitude and location of critical strains induced in the envelope as a result of adhering to a cicada-like nanopattern. This is supported by analysis of micrographs of dead bacteria on a nanopatterned cicada wing surface. The computational analysis is also extended to study different pattern geometries by selectively varying pillar radius, spacing and height, thus informing upon the enhanced design of nanopatterned surfaces.

Materials and Methods

Finite element method

Geometry

The model considered a Gram-negative bacteria interacting with a square array of spherically capped, cylindrical pillars. Several observations were used to reduce the problem, which was otherwise quite convoluted due to the number of pillars and cellular components appearing on the global scale (Figure 1). Firstly, the curvature and global shape change of the cell were ignored, as previously, due to the pillars being over a magnitude smaller than the bacteria (18, 32). Since curvature was negligible, the interaction at each pillar appeared as a repeating event, both in terms of loading and geometry. Hence, it was only necessary to model one representative section with symmetry constraints at the boundaries (Figure 1a,c). Additionally, only cellular components that appeared at, or were directly coupled to, the outermost surface of the bacteria were included in the model. This is due to the nature of the intermolecular forces believed to drive the nanopattern interaction which are finite ranged and thus only engage components in proximity to the contact interface. For a Gram-negative bacteria, this includes the outer membrane and cell wall, which are covalently linked by very abundant lipoproteins that facilitate stress transfer (33-35). The next closest component – the inner membrane - is separated by an isosmotic fluid periplasm making it distant from the other layers and non-load bearing (36). Accordingly, the bacteria was reduced to only an outer membrane and a cell wall (Figure 1b,c).

To model the interaction of these components with a nanopillar, a continuum approach was utilised (Figure 1c). Though the outer membrane and cell wall have been well resolved, the size of the model (10^3-10^4 nm^2) and timescale of adhesion (10-100s) are considered too big for atomistic study (4, 37). Moreover, the present problem involves interactions and contact conditions between structures and components which are challenging to enforce atomistically (38, 39). Therefore, the cell wall and outer membrane were represented as three-dimensional

continuum layers. These layers were defined by a thickness (t_{CW} and t_{OM}, respectively) and a lateral dimension ($s/2$) which was controlled - through symmetry boundary conditions - by the centre-to-centre spacing between pillars (s). Pillars were defined by a diameter (d) or radius (r) and height (h). Initial diameter, spacing and height were set at 60nm, 180nm and 200nm, respectively, to mimic the nanopattern found on the wings of the *Psaltoda claripennis* cicada. Subsequently, dimensions were parametrically varied. Pillar diameter was adjusted between 20-180nm, with the lower bound approaching the maximum resolution of current nanofabrication techniques (30, 40). Dimensionless centre-to-centre spacing (s/d) and height were varied between 2-4 and 100-300nm, respectively.

Material models

By implementing a continuum approach, commonly reported continuum properties such as area compressibility (K_A) and Young's modulus (E) could be invoked to accurately describe the mechanical behavior of the cell wall and outer membrane. Characteristic of biological materials, moduli of these cellular components have large scattering. To account for this, three different envelope configurations were evaluated, covering the softest to the stiffest reported values (Table 1).

An isotopic neo-Hookean material was used to model the constitutive response of the outer membrane, which stems from hydrophobic and van der Waal's forces opposing the separation of lipids. This hyperelastic model is frequently applied to cell membranes (53, 54) and is particularly relevant for bacterial membranes which are known to be strain-softening (33, 55). The material model was informed by previous micropipette aspiration and molecular dynamics studies on bacterial membranes and mimetic lipid systems (33, 41-45). Reported estimates of area compressibility (K_A), Poisson's ratio (v) and thickness (t_{OM}) from a range of these studies are shown in Table 1. These values were used to calculate relevant neo-Hookean parameters (C_{10}, D_1) (Supporting Material A). Evidently, the outer membrane has significant mechanical stiffness, rivalling that of the cell wall, hence both will participate roughly equally in load bearing (34, 56).

The cell wall was modelled as a linear orthotropic material. Though peptidoglycan is thought to be a strain-stiffening biopolymer, an approximately linear response has been observed in many cases, even to rupture (46, 50, 57). Hence, linearity is a good first approximation. Orthotropy was included to account for the directional differences in the stiffness of peptidoglycan which are at least a factor of two (58). This effect stems from the ordered molecular architecture of peptidoglycan, in which rigid glycan strands ($_G$) and flexible peptides stems ($_P$) are covalently crosslinked in a roughly orthogonal fashion (47, 52, 59). A range for the in-plane Young's moduli ($E_1 = E_G$ and $E_2 = E_P$) and Poisson's ratios ($v_{12} = v_{GP}$ and $v_{21} = v_{PG}$) was established by taking values directly from previous studies (Table 1) which include force spectroscopy (46), optical trapping (50), microfluidic bending (49), finite element modelling (48) and atomistic simulation (47, 51). The remaining parameters - namely the shear moduli (G) and out-of-plane Young's modulus (E_3) and Poisson's ratios ($v_{13}, v_{31}, v_{23}, v_{32}$) – were either approximated or inferred (Supporting Material A). For instance, the transverse isotropy of the peptidoglycan network was utilised to reduce the number of unknowns and to infer in-plane properties from corresponding out-of-plane properties. Shear moduli, on the other hand, were approximated using empirically derived formulas and tensor rotation demonstrated previously for analogous, cellular, orthotropic materials (60). In either case, the approximated and inferred properties did not have a significant impact on results. This is most likely due to the nature of the deformation and the small thickness of the cell wall, which emphasise the in-plane Young's moduli. The thickness value (t_{CW}) used in the present study represents roughly two layers of peptidoglycan in the cell wall, which can be between one to three layers thick (2-6nm) depending on the Gram-negative species (46, 47).

Lastly, the pillar was modelled as an infinitely stiff (rigid) material. In some cases, bending of nanopattern features is observed (61). This, however, occurs only in features with low flexural rigidity and only at the cell periphery where adhesion forces have an angled line of action. It is not seen for features which fall under the projected area of the cell, which represent a larger proportion of the contact points. Also, it has not been observed for nanopatterns made of highly stiff materials such as titanium (13) and titanium oxide (30) even when utilising geometrically slender features. Therefore, rigid pillars are well representative.

Interactions

Interactions were applied to define contact relationships between the various components in a manner that was biophysically relevant. There were three such interactions representing surface adhesion, between the pillar and outer leaflet, hydrophobic effects, between the membrane leaflets, and lipoprotein linkages, between the cell wall and inner leaflet (Table 2).

Surface adhesion was modelled as a hard pressure-overclosure, with no separation and rough friction. This dictated that points on the outer leaflet were firmly stuck to the pillar upon contact. Whilst it is known that contact only becomes irreversible after some time, the underlying bond strengthening process unfolds at a rate faster than that at the which the bacteria conforms to the nanopattern (4, 62). Hence, rough friction most correctly describes adhesion. A similar surface-to-surface contact, albeit with no friction, was used for the interaction between membrane leaflets. Thus, the leaflets were allowed to slide over one another, but not to separate. This mimics the hydrophobic forces that hold the leaflets together and oppose only deformation modes that threaten to expose the hydrophobic core. Intermonolayer friction was totally omitted, as it scales with relative velocity which is negligible on the timescale of adhesion (63). Lastly, a tie constraint was used to fuse the inner membrane leaflet to the cell wall, restricting their relative motion. In reality, these envelope components are tightly coupled through covalent lipoprotein linkages which facilitate stress transfer (33, 36). Whilst these are discrete, their very high abundance on the surface of the cell (over 10^6 instances) (64) can be reasonably approximated as a continuous tie constraint. All interaction properties were enforced with more lenient formulations (penalty constraint and surface-to-surface discretization) in order to ease the convergence. Also, use of the more general finite sliding formulation was required.

Elements and mesh

Element selection and mesh generation were optimised to the region-specific deformation modes incurred by the envelope. More specifically, whilst the entire envelope was observed to stretch, albeit nonuniformly, the region in contact with the pillar also incurred bending. Bending requires specific elements and mesh refinement to circumvent hourglass and locking phenomena (65). To allow for this, the envelope was partitioned into an O-grid-like pattern, separating contacting and suspended regions by a relative radius (αr) which is a scalar multiple of the pillar radius (r) (Figure 2)

Contact regions were modelled with first-order, incompatible mode elements (C3D8I) due to their accuracy in bending and efficient elimination of spurious modes via added degrees of freedom and full integration scheme (65). Suspended regions, which remained approximately parallel, were assigned less expensive first-order, reduced integration elements (C3D8R) to optimise computational efficiency. For the outer membrane, which is near incompressible, hybrid formulation (C3D8IH, C3D8RH) was added to avoid volumetric locking (65). Rigid elements (R3D4) were used for the pillar. All parts were meshed with hex elements due to their higher rate of convergence. The hex mesh was generated by a structured mesh approach using local seeds along partitioned edges (A, B, C) as well as through the thickness (T) (Figure 2). The local seeds were controlled to create gradual refinement of the mesh toward the contact region with smooth transitions. Mesh quality was verified using shape metrics. Mesh sensitivity was evaluated to ensure element size was sufficiently small for a converged result (Supporting Material B).

Loading and analysis

For a cell atop a nanopattern, intermolecular adhesion forces are the dominant external force acting in the direction of contact (Figure 3a). Though the cell also experiences weight, its effects are insignificant relative to adhesion forces and the strain limits of the envelope (Supporting Material C). Accordingly, loading was applied to mimic the more critical adhesion forces, which act in an evolving ‘bond front’ due to their finite range (66) (Figure 3b). To capture this, several simulations were run in which a downward pressure load was applied to the bottommost face of the outer leaflet over an area bounded by a relative radius (αr) that was increased incrementally (α= 0.3: 0.1: 2). For each load area, plots of envelope strain energy (U) and adhesion area (A) were generated from the relevant strain energy (ALLSE) and contact area (CAREA) history outputs. The plots were used to calculate the maximum converged strain energy accumulation rate (dU/dA) by fitting a high order polynomial and applying a numerical

differentiation scheme between iterations (Supporting Material D). This rate was used to infer the work of adhesion (W), which is equivalent at equilibrium (i.e. $W=dU/dA$). In other words, adhesion will continue to propagate until the strain work done on the envelope to achieve an incremental increase in contact area equals the corresponding energy released by adhesion (67). By this means, the work of adhesion required to induce a certain level of deformation was estimated.

Monitored outputs and locations

For each load application area, the adhered area, sinking depth and strain conditions corresponding to the maximum equilibrium position were recorded. Adhered area was retrieved from the contact area history output. Sinking depth was measured as the distance from the apex of the pillar tip to the lowest point on the envelope. In-plane uniaxial strains, both circumferential (ε_{11}) and longitudinal (ε_{22}), were probed from the output database. These were then used to also calculate in-plane areal strains ($\varepsilon_A=(1+\varepsilon_{11})(1+\varepsilon_{22})-1$). Both types of strains were monitored at several potentially critical locations (Figure 4a,b) in order to capture the envelope's highly non-uniform deformation. These locations included the pillar apex (L1), the midpoints between two nearest pillars (L2 and L3), and the midpoint between an array of pillars (L4). Classification based on contact (L1) and suspended regions (L2, L3, L4) was also used to coincide with the popular biophysical model (18). For the inner and outer membrane leaflets, values were probed from the top and bottom planes, respectively, corresponding to the position of the hydrophilic headgroups. For the cell wall, maximum values appearing at the top plane were probed (Figure 4b).

The monitored strains were also used to assess physical damage to the envelope via comparison to extensibility limits. Based on previously reported values, the extensibility limit of the cell wall and membrane leaflets was taken to be between $18 < \varepsilon_{22} < 65\%$ (57, 68, 69) and $5 < \varepsilon_A < 35\%$ (70, 71), respectively. Different strain-based failure criteria have been used for the two cell components due to their different molecular architectures, and relatedly, failure mechanisms. For the cell wall, rupture occurs by uniaxial strain, in particular along its longitudinal axis (ε_{22}) which corresponds to the weaker peptide crosslinks (57, 72). For the membrane leaflets, rupture occurs by area increase between hydrophilic headgroups which opens unstable pores (73, 74). In this case, areal strain (ε_A) is more critical than uniaxial strain (71).

Bacterial studies

Sample preparation

Bacterial interaction with a nanopatterned was also studied experimentally using wings of the *Psaltoda Claripennis* cicada. Dried, unmounted cicadas were purchased online (http://www.insectfarm.com.au). Wings were detached and cut into square samples (~10×10mm) for testing. The samples were immobilised onto glass cover slips using small pieces of strategically placed double sided tape to enable removal when required.

Bacterial attachment

A rod-shaped, Gram-negative strain, namely *Pseudomonas aeruginosa* (ATCC 27853) from the American Type Culture Collection (ATCC), was used for the bacterial interaction studies. Before the experiment, bacterial cultures were refreshed on nutrient agar plates (Oxoid). The bacterial cells were grown in 5 mL of sterile nutrient broth at 37 °C with overnight shaking at 180 rpm in an orbital shaker. The bacterial cells were then harvested during the logarithmic phase of growth and the bacterial suspensions adjusted to an OD600 (optical density at 600 nm) of 0.20 in phosphate buffered saline solution as described elsewhere (7). The three wings were immersed in 400µL of bacterial suspension in triplicate in a sterile 48-well polystyrene plate. The surfaces were incubated for 4h at room temperature in an orbital shaker at 80rpm. After incubation, bacteria-adhered surfaces were characterised using fluorescent microscopy to assess viability and scanning electron microscopy to visualise morphology.

Fluorescent microscopy

Viability of adherent *P. aeruginosa* was determined by staining the cells with the LIVE/DEAD® BacLight™ Bacterial Viability kit (Molecular Probes, Invitrogen). The BacLight kit contains 3.3 mM SYTO 9 and 20 mM propidium iodide. Cells were stained for 15 min and imaged for live

(green) and dead cells (red), respectively, after 4h incubation. Fluorescent microscopy was performed using an inverted Nikon Eclipse TI-S microscope. The 40x objective used was a CFI Plan Fluor ELWD ADM 40x with a numerical aperture of 0.6 and working distance of 3.6-2.8 mm, PH2. Ten images of at least three independent replicates were obtained.

Scanning electron microscopy

For visualization by scanning electron microscopy (SEM), the bacterial suspension was removed from the well plates and bacterial cells were fixed on the wing samples using 3% glutaraldehyde (C5H8O2). Fixed samples were then washed in a 0.1 M cacodylate buffer and 1% OsO4, followed by dehydration in a graded ethanol series (from 50 % to 100 %) and drying with hexamethyldisiloxane (C6H19NSi2). Dried samples were then gold coated and mounted. To visualise the underlying deformation and sinking of the bacteria, samples were mounted at a very large incline (~80°) hence images were captured from almost front on, not top down. Two scanning electron microscopes were utilised, one with stage tilt capabilities (JEOL JSM-7001F) and another with in-lens detector, albeit fixed stage (Tescan MIRA3). Both were operated at 5-10keV with a working distance between 5-7mm.

Results and Discussion

Critical action site

Identifying the critical location of envelope deformation is needed to better understand the mechanism of nanopatterned surfaces. This is particularly important given the incompatibility of the longstanding biophysical model with commonly observed tip penetration (11, 28-31). To this effect, Figure 5 shows the evolution of in-plane strains with sinking depth in each envelope layer, at each location of interest, on a cicada-like nanopattern. The nonuniformity of the strain distribution can be inferred from the differing strain levels at each location (Figure 5) and is easily apparent in contour plots of in-plane uniaxial strain (Figure 4b-e).

Accordingly, one or more of these locations was critical for the envelope. Interestingly, however, the critical location of each of the layers did not always coincide. For instance, the outer leaflet of the bilayer membrane experienced maximum areal strain in the suspended region at the centre of an array of pillars (L4) (Figure 5a). Other locations on the outer leaflet either did not experience strain (L1) or experienced tensile strain that was mostly uniaxial (L2, L3) and thus was less critical (71). Conversely, the inner leaflet had its maximum areal (and uniaxial) strain clearly at the pillar apex (L1) (Figure 5b). Moreover, this strain was much higher than that occurring anywhere in the outer leaflet (Figure 5c). This implied that any stretch-induced pore formation and possible rupture of the bilayer would always first initiate within the inner leaflet, at the pillar apex. Similarly, in the cell wall, strains at the pillar apex were significantly larger than at any other location (Figure 5d). Taking these results together, the critical location for both the cell wall and membrane – and thus the envelope overall – was in the contact region precisely at the apex of the pillar tip (L1).

The criticality of the contact region was also confirmed by micrographs of bacteria adhered to the nanopattern of the cicada wing surface (Figure 6). These showed the bacterial envelopes to be compromised at the pillars, whilst regions of the envelope suspended between pillars remained seemingly intact. This could be identified by pillar tips penetrating through the envelope, which corresponded to either partial (Figure 6a) or total (Figure 6b-e) loss of turgor. Moreover, clear penetration seemed to occur shortly after the envelope had sunk below the pillar tip. This is indicated by circular outlines in Figure 6 which highlight examples of penetration where the envelope had sunk to reveal the full spherical dome of the pillar ($p/r \geq \sim 1$). Where the sinking depth was insufficient ($p/r < \sim 1$), there was only perturbation, not penetration, as highlighted by rectangular outlines. This differential deformation could be due to a number of factors, such as the dynamic nature of adhesion and the inhomogeneous surface properties of the bacteria. Most importantly, however, these observations implied that the contact region was critical and that the tip of the pillar delivered high levels of mechanical deformation to the envelope, reinforcing the modelling predictions.

Whilst these findings contradict the prevailing dogma that envelope rupture occurs in the suspended region (18), the criticality of the contact region is not at all surprising. This is due to the nature of the shape change in the contact region, where the envelope is seen to wrap the pillar (Figure 6, rectangular outlines). In doing so, it transforms from an approximately flat plane

into a three-dimensional, non-developable surface. This type of non-developable transformation is notoriously difficult to withstand physically due to double curvature known to generate large tensile membrane strains, in addition to bending strains, at high deflections and rotations, as demonstrated within the model (75, 76). This explains why the suspended region, which remains relatively flat, experiences comparatively lower deformation than the contact region and why penetration, not interstitial tearing, is observed. Consistent with this reasoning and the present findings, observations of tip penetration have also been reported previously on a variety of nanopatterned surfaces. Cicada pillars, gecko spinules (28), dragonfly rods (9), titania wires (30) and black silicon spikes (29), to name a few, have all been seen to penetrate bacterial cells. Additionally, physical penetration is one of the well-established toxicity mechanisms of carbon nanotubes and graphene materials, which can have characteristic dimensions similar to nanopillars (77). For instance, even the thicker multiwalled variants of carbon nanotubes (d = 50nm) can kill cells in this way (78). Accordingly, penetration is likely a common physical mechanism amongst nanoscale materials.

On an additional note, though the outer leaflet did not see comparatively high strains (Figure 5c), it is worthwhile not to dismiss its deformation behaviour. Importantly, this was the only layer in the envelope which behaved as predicted by the biophysical model, having its maximum uniaxial and areal strains in the suspended region (Figure 4e and Figure 5a). Unlike other layers, the outer leaflet directly contacts the pillar and sticks to its surface as a result of bond strengthening and subsequent irreversible adhesion, which was modelled by rough friction (62, 79). The effect is that deformation in the contact region is arrested and instead redistributed to the suspended region. Unsurprisingly, an effectively similar condition is found in the case of the 'biophysical model', which requires adhesion or 'negative adsorption' in order for stretching to be higher in the suspended region. Whilst some level of surface adhesion or sticking is indeed relevant, its impact is easily overestimated if the envelope is simplified as a single layer with small or negligible thickness. This is demonstrated by the outer leaflet, which can be considered a numerical analogue to the analytical solution by Pogodin and others (18) as both involve the adhesion of a single monolayer. However, such simplifications are not accurate for neither Gram-negative nor Gram-positive cells, which have multiple load-bearing layers and significant thickness, respectively. As shown in the present simulation, when the envelope is more accurately modelled as a multilayered structure, the impact of sticking is minimised, and the criticality of the suspended region disappears. Instead, the contact region and pillar apex are revealed to be critical action sites for the envelope, in better agreement with the present experimental observations.

Feasibility of adhesion-driven death

Citing the biophysical model, it is most commonly explained that deformation is driven by passive adhesion forces and that these forces eventually cause death by rupture (18, 24, 29). Problematically, the strength of adhesion forces or bacterial envelopes has not been quantitatively considered. Hence, it remains unclear whether adhesion can induce the levels of deformation commonly observed on nanopatterned surfaces and whether this deformation is sufficient to kill the cell. This has left room for speculations, of varying validity and parsimony, about other forces potentially implicated in nanopattern bactericidal activity (9, 17, 26). To provide quantitative insight, Figure 7 demonstrates the estimated work of adhesion for the deformation of three different Gram-negative envelopes of varying reported stiffness on a cicada-like nanopattern.

To give further meaning to the results, the calculated strains were contextualised with relevant adhesion strengths and envelope extensibilities. As seen in Figure 7a, the cell wall of *Saccharopolyspora erythraea* and *Bacillus subtilis* has been found to rupture at longitudinal uniaxial strains between 18-45% (57, 68) and 35-65% (69, 80), respectively. Similarly, cellulose and chitin – the plant and fungal analogues of peptidoglycan - are known to rupture between 16-35% (81, 82) and 5-10% (83), respectively. As for phospholipid membranes, their areal extensibility is a dynamical property that depends on loading rate (84) and strained area (70). Accordingly, small (~10^2nm^2) mimetic lipid systems strained at fast rates (~10^2mN/m) (as in molecular dynamics simulations) rupture between areal strains of 35-100% (70, 85), whilst large areas loaded quasi-statically (as in micropipette aspiration experiments) rupture between 2-5% (86). In nanopattern interaction, loading is delivered quasi-statically through adhesion and the strained area will at most be localised around the pillar tip (~10^3-10^4nm^2). Accordingly, a plausible critical range at intermediate strains (5-35%) can be defined, and strains reported

from molecular dynamics (>35%) can be considered an absolute upper limit (Figure 7b). For adhesion strength, the van der Waals component can be estimated from the Hamaker constant for bacterial interfaces in aqueous media (typically between $1\text{-}10\times10^{-21}$J) giving 1-10mJ/m^2 at molecular contact (87-89). When additional acid-base interactions are considered, the adhesion strength can be as high as 20-30mJ/m^2 (90, 91), depending on the specific physicochemical properties of the bacteria, interaction medium and substrate.

Based on these values, it is apparent that intrinsic adhesion forces can, in some cases, drive rupture of the envelope. This is most easily appreciated in the case of the soft envelope configuration, which incurred rupture-associated longitudinal and areal strains of 35% in the cell wall and outer membrane, respectively, even at a modest adhesion strength of 10mJ/m^2 (Figure 7a). Furthermore, at this adhesion strength, the sinking depth of the envelope was at a level consistent with rupture observed in micrographs ($p/r\sim1$), as described previously. A similar argument can also be made for the intermediate stiffness envelope, which required 27mJ/m^2 to achieve similar strains and sinking depth, also reasonably within upper reported values for bacterial adhesion. The stiffest envelope, however, did not reach depths seen in micrographs for rupture within 40mJ/m^2, which is uncharacteristically high for bacterial adhesion. Accordingly, all but one of the envelope configurations strongly support adhesion-driven rupture.

The apparent resistance of one of the Gram-negative envelope configurations could quite simply be due to overestimations of mechanical properties and failure criteria. For instance, some previous experimental studies (49, 50) used to inform the material models neglect the additional and comparable stiffness of the outer membrane, hence the reported cell wall stiffness may be overstated up to a factor of two. Similarly, the cited rupture strains are taken from previous experiments existing only for Gram-positive peptidoglycan which is inherently stronger than its Gram-negative counterpart due to increased crosslinking (52). It is also possible that the requirement of total rupture for death may be an overstatement. Envelope stress/strain below rupture-inducing levels, concomitant with lower sinking depths ($p/r<1$) and adhesion energies, may cause other, non-rupture modes of death. For instance, without penetrating through the envelope, it is possible that stretching caused by adhesion is sufficient to sustain several large - otherwise transient – pores, causing osmotic imbalance and subsequent death (77, 92). Additionally, prolonged perturbation and envelope stress may trigger a biochemical cascade of protein, DNA, and oxidative damage as seen in the so-called ‘wrapping’ mechanism of carbon nanotubes and graphene materials which does not require explicit penetration (93, 94). Penetration and wrapping mechanisms of these carbon-based nanoscale materials are also believed to be driven by intermolecular adhesion forces, predominantly van der Waals (93) and electrostatic (95). These additional mechanical - or mechanically triggered modes - may explain the occurrence of non-visibly-penetrated cells on the cicada wing surface (Figure 6f), which were also presumably compromised based on the overwhelming proportion of dead cells in fluorescence microscopy images (Figure S4 in the Supporting Material). In light of these possible overestimations and less pronounced death modes, the numerical results overall reaffirm adhesion-driven deformation and death, as originally posited by Pogodin and others (18).

Effects of geometry

The level of deformation and death induced through adhesion is expected to depend on the geometry of the nanopattern. Whilst this notion seems relatively intuitive, the effects of even broad geometric parameters such as radius, spacing and height are still not systematically understood (10, 22). To provide clearer insight, Figure 8 demonstrates the impact of pillar radius and spacing on the maximum uniaxial and areal strain in the envelope. For all geometries studied, maximums of uniaxial and areal strain in the cell wall and outer membrane appeared consistently at the pillar apex. Also, the global maximum for the envelope was at the pillar apex, in the cell wall.

Decreasing radius and spacing increased the maximum uniaxial and areal strain in the envelope. For radius (Figure 8a), the effect was quite pronounced. At an adhesion energy of 10mJ/m^2, decreasing radius from 30-10nm increased maximum envelope strain by approximately 25%, whilst increasing radius from 30-90nm produced a reduction of approximately 10-15%. Spacing, on the other hand, had a less significant impact on maximum strain (Figure 8b). Its effects only appeared at higher adhesion energies and sinking depths.

Plots of maximum uniaxial and areal strain for all three spacings (120, 180, 240nm) were coincident up to about 10mJ/m^2, indicating that there was effectively no variation in maximum envelope strain. At 20mJ/m^2, however, some deviation could be observed, most noticeably in terms of maximum areal strain which increased by 5% with a reduction in spacing from 240-120nm.

The trend with radius is in good agreement with previous literature. Increased killing efficiency against bacteria with thinner or sharper pillars is a common experimental observation (10, 13, 96). For instance, investigating the bactericidal performance of three cicada species against Gram-negative bacteria, Kelleher and others (22) found that the species with the smallest radius produced the highest killing efficiency. Similarly, Michalska and others (29) also demonstrated that sharper tipped black silicon pillars were more effective than blunt counterparts against a range of Gram-negative and Gram-positive bacteria. In both studies, however, changes to pillar radius were coupled to height and spacing, hence conclusions on the impact of any parameters individually have so far been limited. In combination with the present modelling, however, the role of radius is more convincing. Its impact can be straightforwardly interpreted as a stress concentration, which intensifies stress/strain in the contact region due to reduced contact area. More accurately, however, the effect of radius is due to curvature ($1/r$), which is proportional to the membrane and bending strains produced by the non-developable transformation of the envelope in the contact region (75). Accordingly, refining the pillar tip radius can be recommended to enhance bactericidal efficiency.

Comparatively, the role of spacing is not so straight forward. Sensitivity to spacing in the present study can be attributed to stress distributions overlapping and compounding as neighbouring pillars are brought closer, thus increasing the maximum strain in the envelope. This effect, however, is weak in comparison to radius because the critical deformation and maximum strain occur at the pillar apex. Interestingly, however, some other theoretical studies have reported a strong spacing sensitivity, with a contradictory trend. In their respective analytical and finite element models, Xue and others (27) and Mirzaali and others (26) demonstrated that larger spacing increased the maximum deformation of the envelope. Both models, however, considered the weight of the cell to be the driving force behind the interaction. Not only is weight a trivial load (Supporting Material C), but it is also conceptually misrepresentative. Weight, or any other 'constant' load, will always produce a straightforward sensitivity to spacing resulting from the distribution of that load over a given number of pillars or contact points. This is similar to how a bed of nails becomes injurious once the nails are distantly separated. The case of bacteria on a nanopattern, however, is a very different scenario. Interaction forces develop individually at each pillar. This phenomenon can be observed in micrographs, specifically at the periphery of cells where pillars are 'pulled' into contact (Figure 8c). Accordingly, reducing spacing should not adversely affect maximum stress/strain, and should only enhance it, as demonstrated presently. Spacing also has another important role, distinct from maximum strain - that is, controlling the number of contact points. Whilst there is only a small (at most 5%) increase in maximum strain by reducing spacing from 240nm to 120nm, the pillar density and number of contact points increase by a factor of four (Figure 8d). Having increased contact points enables more envelope damage to be delivered over the cell. It also increases the chances of localised tip rupture, given that bacteria are known to have mechanical properties and adhesive biopolymer concentrations varying spatially across their surface (91, 97). The present results indicate that spacing can be safely reduced to increase the number of contact points without detriment to maximum stress/strain, unlike suggested previously. Importantly, this recommendation is more consistent with experimental trends. Across several studies involving black silicon (16, 96) , polymer (10), and insect wings (22, 23), more closely spaced pillars have exhibited enhanced killing efficiency, though direct conclusions were again precluded by simultaneous changes to radius and height. More recently, however, a study by electron beam induced deposition clearly demonstrated enhanced killing efficiency against Gram-positive bacteria resulting from selective spacing reduction (98). Taking these experimental observations together with the present modelling, it can be strongly recommended that reducing spacing increases killing efficiency.

Effects of height were not explicitly shown. Beyond the value needed to allow sufficient sinking ($\sim h/r>1$), height was totally inconsequential to the deformation of the envelope. In contrast, an interest in height has been popular in the literature, tracing back to early reports of increased killing efficiency correlated to higher pillar 'aspect ratios' (22, 29). Several possible explanations

can be offered for these observations. For example, some authors have suggested that height may have an effect indirectly via adhesion energy (23). As shown by the surface element integration technique, pillars can drastically reduce the repulsive interaction energy barrier commonly seen in bacterial adhesion by separating the cell from the bulk of the underlying substrate (99). However, these effects should only be present for pillar heights within the range of intermolecular forces (at the very most 50nm), whilst pillars are typically much taller (100-1000nm). This is consistent with a recent study which found similar adhesion forces for pillars between 220 – 420nm tall, with the same diameter and spacing (61). It has also been postulated that taller pillars may be more bactericidal due to their reduced flexural rigidity which causes increased deflection under equivalent interaction forces (17, 61). According to this theory, elastic strain energy stored in the pillars through deflection may lead to increased envelope stretching. Problematically, modelling of the direct link between the pillar deflection and the resulting envelope stress/strain is totally absent. Moreover, it can be argued that this link is not convincing. For one, the deflection of pillars – which typically bend towards the cell (Figure 8c) – would effectively reduce the distance the envelope must stretch in order to come into contact. More importantly, the intermolecular forces which cause pillar bending are not removed upon contact, therefore the bent pillars would not exert their stored 'springback' energy upon the envelope, as has been suggested (61). And lastly, bent pillars tend to be confined to the cell periphery. Though having boundary conditions that are poorly defined, this region of the envelope is evidently less constrained and therefore presumably less critical. Also, overall, the significance of bent pillars is questionable as proportionally more contact points occur underneath the projected area of the cell where the pillars remain upright (Figure 6b). Accordingly, height-modulated killing efficiency is not strongly explained by the existing deflection theory. A final explanation is that changes to pillar height have often been accompanied by changes to radius, which is overlooked when descriptions of 'aspect ratio' are used (22, 29). The variable efficiency in these studies may have been solely due to the reduction in radius and not related to height whatsoever. Albeit relatively unexciting, this suggestion bodes well with the present research, which finds smaller radii pillars significantly enhance envelope stress/strain whilst pillar height has no such effect. With no clear role of height from a theoretical perspective, including the present work, radius and spacing are more effective design parameters for enhancing killing efficiency.

Mechanism updates and perspectives

Combining the various aspects of the present work, an updated mechanism for bactericidal activity on nanopatterned surfaces can be put forth. Accordingly, nanopatterned surfaces kill bacteria by eliciting significant deformation through contact, which is driven by intermolecular adhesion forces acting locally between the pillars and the bacteria. This deformation may occasion death in a number of ways, ranging from relatively inconspicuous DNA, oxidative or protein damage to highly pronounced physical rupture. In either case, deformation is critical at the pillar apex, due to the non-developable shape transformation of the envelope around pillar tips which induces significant in-plane strains. When these strains exceed the tensile limits of cell wall and outer membrane, a tip-localised rupture occurs and presents itself in a manner resembling penetration, with pillars protruding through the cell. The killing efficiency for such a mechanism can be enhanced by reduction to pillar radius and spacing, which intensify the maximum strain and increase the frequency of perturbation points, respectively.

This tip-localised mechanism is expected to dominate a significant proportion of cell-nanopattern interactions. For instance, based on the geometries studied, all nanopatterned surfaces having a dimensionless spacing ratio greater than two will kill Gram-negative bacteria predominantly in this way. This range captures a large population of previously reported bactericidal nanopatterns, both natural – such as cicada wings (22) and gecko skin (11) – and synthetic – such as those fabricated by reactive ion etching (29, 100), electron beam lithography (13) and nanoimprint lithography (10). Also, a tip-localised mechanism seems more compatible with the killing effect of certain disordered nanostructures with variable heights, such as dragonfly wings (9) and hydrothermally synthesised nanowires (30, 31). Due to their nonuniformity, these create only a few discrete contact points which are unlikely to cause significant interstitial stretching. As for different cell types, the present mechanism is plausible, but ultimately requires further investigation. Gram-positive and eukaryotic cells have distinctly different physical structures which would significantly impact the deformation mechanics. Gram-positive bacteria, for instance, do not contain an outer membrane and instead have cell walls

up to 80nm thick. Their cell walls are also under a high, non-negligible initial strain, due to significant turgor pressure. For eukaryotic cells, the outer membrane is attached to, and supported by, a cytoskeleton which pervades through the cell. In this case, a model of isolated layers may not be sufficiently accurate. That being said, certain trends from the present study do seem to align with the behaviour of these cells on nanopatterned surfaces, both of which have reported instances of enhanced resistance (19, 20, 30). For Gram-positive cells, this can be explained straightforwardly due to their thickness, which increases envelope stiffness. For eukaryotic cells, this could be due in part to the inclusion of cholesterol in their lipid membrane which increases both stiffness and extensibility - relative to pure phospholipid membranes - by at least a factor of two to three (74). As shown in Figure 7, increased stiffness and extensibility limits would indeed lead to greater survivability. Also, both cells become susceptible when subjected to nanopatterns with very small radii (8), as has been suggested in Figure 8. Whilst the mechanism is indeed compatible with these trends, studies with more appropriate cell models are ultimately required before their failure mode can be confidently elucidated.

Conclusions

Valuable insights to the mechanism of nanopatterned surfaces lie behind accurate descriptions of contact and interaction mechanics. This has been demonstrated in the present work through computational modelling of bacteria-nanopattern adhesion with carefully considered multilayer structure, interaction properties and boundary conditions. By this approach, improved understanding of the critical action site and geometric enhancement of nanopatterned surfaces has been derived. It is now understood that non-developable deformation about pillar tips can produce critical strains at the pillar apex, which may locally rupture and penetrate through the bacteria. Bactericidal activity by this effect can be enhanced through reduction to pillar radius and spacing, which increase the magnitude of maximum strains and the frequency of perturbation points, respectively. These findings can immediately help toward the design of nanopatterned surfaces with enhanced bactericidal efficiency and may offer a starting point for cytocompatibility studies in the future. Nanopatterned surfaces exhibiting both properties are ultimately needed in order to progress this promising technology through the development pipeline.

Author Contributions

All authors made significant scientific contributions to the reported work. A.V. conceptualised and designed the research, performed computational modelling and microscopy, analysed the data, prepared figures and tables and wrote the manuscript. J.H. performed microscopy and reviewed the manuscript. Z.L. and P.K.D.V.Y. provided ongoing technical and high-level expertise to all aspects and reviewed the manuscript.

Acknowledgments

This work was enabled by research facilities at the Queensland University of Technology (QUT), including the Central Analytical Research Facility (CARF) - hosted by the Institute for Future Environments (IFE) - the Institute of Health and Biomedical Innovation (IHBI) and the High Perforcemance Computing (HPC) facility. Funding was provided through the Queensland University of Technology (QUT) Research Training Program (RTP) stipend. The authors declare that they have no affiliations with or involvement in any private-sector organisations or entities with financial conflicts of interests.

References

1. Penesyan, A., M. Gillings, and I. Paulsen. 2015. Antibiotic Discovery: Combatting Bacterial Resistance in Cells and in Biofilm Communities. Molecules 20(4):5286.

2. Pidot, S. J., W. Gao, A. H. Buultjens, I. R. Monk, R. Guerillot, G. P. Carter, J. Y. H. Lee, M. M. C. Lam, M. L. Grayson, S. A. Ballard, A. A. Mahony, E. A. Grabsch, D. Kotsanas, T. M. Korman, G. W. Coombs, J. O. Robinson, A. Gonçalves da Silva, T. Seemann, B. P. Howden, P. D. R. Johnson, and T. P. Stinear. 2018. Increasing tolerance of hospital Enterococcus faecium to handwash alcohols. Science translational medicine 10(452).

3. Huh, A. J., and Y. J. Kwon. 2011. "Nanoantibiotics": a new paradigm for treating infectious diseases using nanomaterials in the antibiotics resistant era. Journal of controlled release : official journal of the Controlled Release Society 156(2):128-145.

4. Ivanova, E. P., J. Hasan, H. K. Webb, V. K. Truong, G. S. Watson, J. A. Watson, V. A. Baulin, S. Pogodin, J. Y. Wang, M. J. Tobin, C. Löbbe, and R. J. Crawford. 2012. Natural Bactericidal Surfaces: Mechanical Rupture of Pseudomonas aeruginosa Cells by Cicada Wings. Small 8(16):2489-2494.

5. Bhadra, C. M., V. Khanh Truong, V. T. H. Pham, M. Al Kobaisi, G. Seniutinas, J. Y. Wang, S. Juodkazis, R. J. Crawford, and E. P. Ivanova. 2015. Antibacterial titanium nano-patterned arrays inspired by dragonfly wings. Scientific Reports 5:16817. Article.

6. Hasan, J., S. Jain, R. Padmarajan, S. Purighalla, V. K. Sambandamurthy, and K. Chatterjee. 2018. Multi-scale surface topography to minimize adherence and viability of nosocomial drug-resistant bacteria. Materials & Design 140:332-344.

7. Hasan, J., Y. Xu, T. Yarlagadda, M. Schuetz, K. Spann, and P. K. D. V. Yarlagadda. 2020. Antiviral and Antibacterial Nanostructured Surfaces with Excellent Mechanical Properties for Hospital Applications. ACS Biomaterials Science & Engineering.

8. Hasan, J., S. Raj, L. Yadav, and K. Chatterjee. 2015. Engineering a nanostructured "super surface" with superhydrophobic and superkilling properties. RSC Advances 5(56):44953-44959. 10.1039/C5RA05206H.

9. Bandara, C. D., S. Singh, I. O. Afara, A. Wolff, T. Tesfamichael, K. Ostrikov, and A. Oloyede. 2017. Bactericidal Effects of Natural Nanotopography of Dragonfly Wing on Escherichia coli. ACS Applied Materials & Interfaces 9(8):6746-6760.

10. Dickson, M. N., E. I. Liang, L. A. Rodriguez, N. Vollereaux, and A. F. Yee. 2015. Nanopatterned polymer surfaces with bactericidal properties. Biointerphases 10(2):021010.

11. Green, D. W., K. K.-H. Lee, J. A. Watson, H.-Y. Kim, K.-S. Yoon, E.-J. Kim, J.-M. Lee, G. S. Watson, and H.-S. Jung. 2017. High Quality Bioreplication of Intricate Nanostructures from a Fragile Gecko Skin Surface with Bactericidal Properties. Scientific Reports 7:41023. Article.

12. Jaggessar, A., A. Mathew, H. Wang, T. Tesfamichael, C. Yan, and P. K. D. V. Yarlagadda. 2018. Mechanical, bactericidal and osteogenic behaviours of hydrothermally synthesised TiO2 nanowire arrays. Journal of the Mechanical Behavior of Biomedical Materials 80:311-319.

13. Shahali, H., J. Hasan, A. Mathews, H. Wang, C. Yan, T. Tesfamichael, and P. K. D. V. Yarlagadda. 2019. Multi-biofunctional properties of three species of cicada wings and biomimetic fabrication of nanopatterned titanium pillars. Journal of Materials Chemistry B 7(8):1300-1310. 10.1039/C8TB03295E.

14. Bruzaud, J., J. Tarrade, E. Celia, T. Darmanin, E. Taffin de Givenchy, F. Guittard, J.-M. Herry, M. Guilbaud, and M.-N. Bellon-Fontaine. 2017. The design of superhydrophobic stainless steel surfaces by controlling nanostructures: A key parameter to reduce the implantation of pathogenic bacteria. Materials Science and Engineering: C 73:40-47.

15. Ivanova, E. P., J. Hasan, H. K. Webb, G. Gervinskas, S. Juodkazis, V. K. Truong, A. H. F. Wu, R. N. Lamb, V. A. Baulin, G. S. Watson, J. A. Watson, D. E. Mainwaring, and

R. J. Crawford. 2013. Bactericidal activity of black silicon. Nature Communications 4:2838. Article.

16. Bhadra, C. M., M. Werner, V. A. Baulin, V. K. Truong, M. A. Kobaisi, S. H. Nguyen, A. Balcytis, S. Juodkazis, J. Y. Wang, D. E. Mainwaring, R. J. Crawford, and E. P. Ivanova. 2018. Subtle Variations in Surface Properties of Black Silicon Surfaces Influence the Degree of Bactericidal Efficiency. Nano-Micro Letters 10(2):36.

17. Linklater, D. P., M. De Volder, V. A. Baulin, M. Werner, S. Jessl, M. Golozar, L. Maggini, S. Rubanov, E. Hanssen, S. Juodkazis, and E. P. Ivanova. 2018. High Aspect Ratio Nanostructures Kill Bacteria via Storage and Release of Mechanical Energy. ACS Nano.

18. Pogodin, S., J. Hasan, Vladimir A. Baulin, Hayden K. Webb, Vi K. Truong, The H. Phong Nguyen, V. Boshkovikj, Christopher J. Fluke, Gregory S. Watson, Jolanta A. Watson, Russell J. Crawford, and Elena P. Ivanova. 2013. Biophysical Model of Bacterial Cell Interactions with Nanopatterned Cicada Wing Surfaces. Biophysical Journal 104(4):835-840.

19. Hasan, J., H. K. Webb, V. K. Truong, S. Pogodin, V. A. Baulin, G. S. Watson, J. A. Watson, R. J. Crawford, and E. P. Ivanova. 2013. Selective bactericidal activity of nanopatterned superhydrophobic cicada Psaltoda claripennis wing surfaces. Applied Microbiology and Biotechnology 97(20):9257-9262.

20. Hasan, J., S. Jain, and K. Chatterjee. 2017. Nanoscale Topography on Black Titanium Imparts Multi-biofunctional Properties for Orthopedic Applications. Scientific Reports 7:41118. Article.

21. Hasan, J., R. J. Crawford, and E. P. Ivanova. 2013. Antibacterial surfaces: the quest for a new generation of biomaterials. Trends in Biotechnology 31(5):295-304.

22. Kelleher, S. M., O. Habimana, J. Lawler, B. O'Reilly, S. Daniels, E. Casey, and A. Cowley. 2016. Cicada Wing Surface Topography: An Investigation into the Bactericidal Properties of Nanostructural Features. ACS Applied Materials and Interfaces 8(24):14966-14974.

23. Nowlin, K., A. Boseman, A. Covell, and D. LaJeunesse. 2015. Adhesion-dependent rupturing of Saccharomyces cerevisiae on biological antimicrobial nanostructured surfaces. Journal of the Royal Society Interface 12(102):20140999.

24. Elbourne, A., J. Chapman, A. Gelmi, D. Cozzolino, R. J. Crawford, and V. K. Truong. 2019. Bacterial-nanostructure interactions: The role of cell elasticity and adhesion forces. Journal of Colloid and Interface Science 546:192-210.

25. Li, X. 2016. Bactericidal mechanism of nanopatterned surfaces. Physical Chemistry Chemical Physics 18(2):1311-1316. 10.1039/C5CP05646B.

26. Mirzaali, M. J., I. C. P. v. Dongen, N. Tümer, H. Weinans, S. A. Yavari, and A. A. Zadpoor. 2018. In-silico quest for bactericidal but non-cytotoxic nanopatterns. Nanotechnology 29(43):43LT02.

27. Xue, F., J. Liu, L. Guo, L. Zhang, and Q. Li. 2015. Theoretical study on the bactericidal nature of nanopatterned surfaces. Journal of Theoretical Biology 385:1-7.

28. Watson, G. S., D. W. Green, J. A. Watson, Z. Zhou, X. Li, G. S. P. Cheung, and M. Gellender. 2019. A Simple Model for Binding and Rupture of Bacterial Cells on Nanopillar Surfaces. Advanced Materials Interfaces 6(10):1801646.

29. Michalska, M., F. Gambacorta, R. Divan, I. S. Aranson, A. Sokolov, P. Noirot, and P. D. Laible. 2018. Tuning antimicrobial properties of biomimetic nanopatterned surfaces. Nanoscale 10(14):6639-6650. 10.1039/C8NR00439K.

30. Jaggessar, A., A. Mathew, T. Tesfamichael, H. Wang, C. Yan, and P. K. Yarlagadda. 2019. Bacteria Death and Osteoblast Metabolic Activity Correlated to Hydrothermally Synthesised TiO_2 Surface Properties. Molecules (Basel, Switzerland) 24(7):1201.

31. Diu, T., N. Faruqui, T. Sjöström, B. Lamarre, H. F. Jenkinson, B. Su, and M. G. Ryadnov. 2014. Cicada-inspired cell-instructive nanopatterned arrays. Scientific Reports 4:7122. Article.

32. Christian, D., A. Miglena, and P. Bernard. 1997. Adhesion of Latex Spheres to Giant Phospholipid Vesicles: Statics and Dynamics. J. Phys. II France 7(11):1651-1682. 10.1051/jp2:1997208.

33. Hwang, H., N. Paracini, J. M. Parks, J. H. Lakey, and J. C. Gumbart. 2018. Distribution of mechanical stress in the Escherichia coli cell envelope. Biochimica et Biophysica Acta (BBA) - Biomembranes 1860(12):2566-2575.

34. Rojas, E. R., G. Billings, P. D. Odermatt, G. K. Auer, L. Zhu, A. Miguel, F. Chang, D. B. Weibel, J. A. Theriot, and K. C. Huang. 2018. The outer membrane is an essential load-bearing element in Gram-negative bacteria. Nature 559(7715):617-621.

35. Samsudin, F., A. Boags, T. J. Piggot, and S. Khalid. 2017. Braun's Lipoprotein Facilitates OmpA Interaction with the Escherichia coli Cell Wall. Biophysical Journal 113(7):1496-1504.

36. Erickson, H. P. 2017. How bacterial cell division might cheat turgor pressure – a unified mechanism of septal division in Gram-positive and Gram-negative bacteria. 39(8):1700045.

37. Groot, R. D., and K. L. Rabone. 2001. Mesoscopic simulation of cell membrane damage, morphology change and rupture by nonionic surfactants. Biophysical journal 81(2):725-736.

38. Kamm, R., A. K. McVittie, and M. Bathe. 2000. On the role of continuum models in mechanobiology. ASME Applied Mechanics Division-Publications-AMD 242:1-12.

39. Tang, Y., G. Cao, X. Chen, J. Yoo, A. Yethiraj, and Q. Cui. 2006. A Finite Element Framework for Studying the Mechanical Response of Macromolecules: Application to the Gating of the Mechanosensitive Channel MscL. Biophysical Journal 91(4):1248-1263.

40. Cattoni, A., J. Chen, D. Decanini, J. Shi, A.-M. J. R. A. i. N. T. Haghiri-Gosnet, and Applications. 2011. Soft UV nanoimprint lithography: a versatile tool for nanostructuration at the 20nm scale.139-156.

41. Nakayama, Y., K. Komazawa, N. Bavi, K.-i. Hashimoto, H. Kawasaki, and B. Martinac. 2018. Evolutionary specialization of MscCG, an MscS-like mechanosensitive channel, in amino acid transport in Corynebacterium glutamicum. Scientific Reports 8(1):12893.

42. Sun, Y., T.-L. Sun, and Huey W. Huang. 2014. Physical Properties of Escherichia coli Spheroplast Membranes. Biophysical Journal 107(9):2082-2090.

43. Rawicz, W., K. C. Olbrich, T. McIntosh, D. Needham, and E. Evans. 2000. Effect of Chain Length and Unsaturation on Elasticity of Lipid Bilayers. Biophysical Journal 79(1):328-339.

44. Terzi, M. M., M. Deserno, and J. F. Nagle. 2019. Mechanical properties of lipid bilayers: a note on the Poisson ratio. Soft Matter 15(44):9085-9092. 10.1039/C9SM01290G.

45. Shahane, G., W. Ding, M. Palaiokostas, and M. Orsi. 2019. Physical properties of model biological lipid bilayers: insights from all-atom molecular dynamics simulations. Journal of Molecular Modeling 25(3):76.

46. Yao, X., M. Jericho, D. Pink, and T. Beveridge. 1999. Thickness and elasticity of gram-negative murein sacculi measured by atomic force microscopy. Journal of bacteriology 181(22):6865-6875.

47. Gumbart, J. C., M. Beeby, G. J. Jensen, and B. Roux. 2014. Escherichia coli Peptidoglycan Structure and Mechanics as Predicted by Atomic-Scale Simulations. PLOS Computational Biology 10(2):e1003475.

48. Deng, Y., M. Sun, and J. W. Shaevitz. 2011. Direct Measurement of Cell Wall Stress Stiffening and Turgor Pressure in Live Bacterial Cells. Physical Review Letters 107(15):158101.

49. Auer, George K., Timothy K. Lee, M. Rajendram, S. Cesar, A. Miguel, Kerwyn C. Huang, and Douglas B. Weibel. 2016. Mechanical Genomics Identifies Diverse Modulators of Bacterial Cell Stiffness. Cell Systems 2(6):402-411.

50. Amir, A., F. Babaeipour, D. B. McIntosh, D. R. Nelson, and S. Jun. 2014. Bending forces plastically deform growing bacterial cell walls. Proceedings of the National Academy of Sciences 111(16):5778.

51. Assidi, M., F. Dos Reis, and J. F. Ganghoffer. 2011. Equivalent mechanical properties of biological membranes from lattice homogenization. Journal of the Mechanical Behavior of Biomedical Materials 4(8):1833-1845.

52. Gan, L., S. Chen, and G. J. Jensen. 2008. Molecular organization of Gram-negative peptidoglycan. Proceedings of the National Academy of Sciences of the United States of America 105(48):18953-18957.

53. Bavi, N., Y. Nakayama, O. Bavi, C. D. Cox, Q.-H. Qin, and B. Martinac. 2014. Biophysical implications of lipid bilayer rheometry for mechanosensitive channels. Proceedings of the National Academy of Sciences of the United States of America 111(38):13864-13869.

54. Yoon, D., and D. You. 2016. Continuum modeling of deformation and aggregation of red blood cells. Journal of Biomechanics 49(11):2267-2279.

55. Rawicz, W., B. A. Smith, T. J. McIntosh, S. A. Simon, and E. Evans. 2008. Elasticity, Strength, and Water Permeability of Bilayers that Contain Raft Microdomain-Forming Lipids. Biophysical Journal 94(12):4725-4736.

56. Wong, F., and A. Amir. 2019. Mechanics and Dynamics of Bacterial Cell Lysis. Biophysical Journal 116(12):2378-2389.

57. Stocks, S. M., and C. R. Thomas. 2001. Strength of mid-logarithmic and stationary phase Saccharopolyspora erythraea hyphae during a batch fermentation in defined nitrate-limited medium. Biotechnology and Bioengineering 73(5):370-378.

58. Tavaddod, S., and H. Naderi-Manesh. 2016. In Vivo study of naturally deformed Escherichia coli bacteria. Journal of Bioenergetics and Biomembranes 48(3):281-291.

59. Vollmer, W., and J.-V. Höltje. 2004. The Architecture of the Murein (Peptidoglycan) in Gram-Negative Bacteria: Vertical Scaffold or Horizontal Layer(s)? Journal of Bacteriology 186(18):5978.

60. Bachtiar, E. V., M. Rüggeberg, S. Hering, M. Kaliske, and P. Niemz. 2017. Estimating shear properties of walnut wood: a combined experimental and theoretical approach. Materials and Structures 50(6):248.

61. Ivanova, E. P., D. P. Linklater, M. Werner, V. A. Baulin, X. Xu, N. Vrancken, S. Rubanov, E. Hanssen, J. Wandiyanto, V. K. Truong, A. Elbourne, S. Maclaughlin, S. Juodkazis, and R. J. Crawford. 2020. The multi-faceted mechano-bactericidal mechanism of nanostructured surfaces. Proceedings of the National Academy of Sciences:201916680.

62. Boks, N. P., H. J. Busscher, H. C. van der Mei, and W. Norde. 2008. Bond-Strengthening in Staphylococcal Adhesion to Hydrophilic and Hydrophobic Surfaces Using Atomic Force Microscopy. Langmuir 24(22):12990-12994.

63. Shkulipa, S. A., W. K. den Otter, and W. J. Briels. 2006. Thermal Undulations of Lipid Bilayers Relax by Intermonolayer Friction at Submicrometer Length Scales. Physical Review Letters 96(17):178302.

64. Braun, V., and K. Hantke. 2019. Lipoproteins: Structure, Function, Biosynthesis. Bacterial Cell Walls and Membranes. A. Kuhn, editor. Springer International Publishing, Cham, pp. 39-77.

65. Dassault Systèmes Simulia Corp. 2016. ABAQUS Online Documentation.

66. Turner, K. T., and S. M. Spearing. 2002. Modeling of direct wafer bonding: Effect of wafer bow and etch patterns. Journal of Applied Physics 92(12):7658-7666.

67. Ciavarella, M., J. Joe, A. Papangelo, and J. R. Barber. 2019. The role of adhesion in contact mechanics. Journal of The Royal Society Interface 16(151):20180738.

68. Stocks, S. M., and C. R. Thomas. 2001. Viability, strength, and fragmentation of Saccharopolyspora erythraea in submerged fermentation. Biotechnology and Bioengineering 75(6):702-709.

69. Thwaites, J. J., U. C. Surana, and A. M. Jones. 1991. Mechanical properties of Bacillus subtilis cell walls: effects of ions and lysozyme. Journal of Bacteriology 173(1):204.

70. Tolpekina, T. V., W. K. den Otter, and W. J. Briels. 2004. Simulations of stable pores in membranes: System size dependence and line tension. The Journal of Chemical Physics 121(16):8014-8020.

71. Li, F., C. U. Chan, and C. D. Ohl. 2013. Yield strength of human erythrocyte membranes to impulsive stretching. Biophysical journal 105(4):872-879.

72. Mendelson, N. H., and J. J. Thwaites. 1989. Cell wall mechanical properties as measured with bacterial thread made from Bacillus subtilis. Journal of bacteriology 171(2):1055-1062.

73. Koshiyama, K., and S. Wada. 2011. Molecular dynamics simulations of pore formation dynamics during the rupture process of a phospholipid bilayer caused by high-speed equibiaxial stretching. Journal of Biomechanics 44(11):2053-2058.

74. Shigematsu, T., K. Koshiyama, and S. Wada. 2015. Effects of Stretching Speed on Mechanical Rupture of Phospholipid/Cholesterol Bilayers: Molecular Dynamics Simulation. Scientific reports 5:15369-15369.

75. Majidi, C., and R. S. Fearing. 2008. Adhesion of an Elastic Plate to a Sphere. Proceedings: Mathematical, Physical and Engineering Sciences 464(2093):1309-1317.

76. Reddy, J. N. 2006. Theory and analysis of elastic plates and shells. CRC press.

77. Zou, X., L. Zhang, Z. Wang, and Y. Luo. 2016. Mechanisms of the Antimicrobial Activities of Graphene Materials. Journal of the American Chemical Society 138(7):2064-2077.

78. Nagai, H., Y. Okazaki, S. H. Chew, N. Misawa, Y. Yamashita, S. Akatsuka, T. Ishihara, K. Yamashita, Y. Yoshikawa, H. Yasui, L. Jiang, H. Ohara, T. Takahashi, G. Ichihara, K. Kostarelos, Y. Miyata, H. Shinohara, and S. Toyokuni. 2011. Diameter and rigidity of multiwalled carbon nanotubes are critical factors in mesothelial injury and carcinogenesis. Proceedings of the National Academy of Sciences 108(49):E1330.

79. van der Mei, H. C., M. Rustema-Abbing, J. de Vries, and H. J. Busscher. 2008. Bond Strengthening in Oral Bacterial Adhesion to Salivary Conditioning Films. Applied and Environmental Microbiology 74(17):5511.

80. Ye, X., L. Zhao, J. Liang, X. Li, and G.-Q. Chen. 2017. Study of the tensile properties of individual multicellular fibres generated by Bacillus subtilis. Scientific reports 7:46052-46052.

81. Chen, S.-Q., P. Lopez-Sanchez, D. Wang, D. Mikkelsen, and M. J. Gidley. 2018. Mechanical properties of bacterial cellulose synthesised by diverse strains of the genus Komagataeibacter. Food Hydrocolloids 81:87-95.

82. Costa, A. F. S., F. C. G. Almeida, G. M. Vinhas, and L. A. Sarubbo. 2017. Production of Bacterial Cellulose by Gluconacetobacter hansenii Using Corn Steep Liquor As Nutrient Sources. 8(2027). Original Research.

83. Cui, J., Z. Yu, and D. Lau. 2016. Effect of Acetyl Group on Mechanical Properties of Chitin/Chitosan Nanocrystal: A Molecular Dynamics Study. Int J Mol Sci 17(1):61.

84. Evans, E., V. Heinrich, F. Ludwig, and W. Rawicz. 2003. Dynamic Tension Spectroscopy and Strength of Biomembranes. Biophysical Journal 85(4):2342-2350.

85. Saeedimasine, M., A. Montanino, S. Kleiven, and A. Villa. 2019. Role of lipid composition on the structural and mechanical features of axonal membranes: a molecular simulation study. Scientific reports 9(1):8000-8000.

86. Needham, D., and R. S. Nunn. 1990. Elastic deformation and failure of lipid bilayer membranes containing cholesterol. Biophysical journal 58(4):997-1009.

87. Israelachvili, J. N. 2011. Intermolecular and Surface Forces. Academic Press.

88. van der Westen, R., J. Sjollema, R. Molenaar, P. K. Sharma, H. C. van der Mei, and H. J. Busscher. 2018. Floating and Tether-Coupled Adhesion of Bacteria to Hydrophobic and Hydrophilic Surfaces. Langmuir : the ACS journal of surfaces and colloids 34(17):4937-4944.

89. Gentile, G. J., M. C. Cruz, V. B. Rajal, and M. M. Fidalgo de Cortalezzi. 2018. Electrostatic interactions in virus removal by ultrafiltration membranes. Journal of Environmental Chemical Engineering 6(1):1314-1321.

90. Zhang, X., Q. Zhang, T. Yan, Z. Jiang, X. Zhang, and Y. Y. Zuo. 2015. Quantitatively Predicting Bacterial Adhesion Using Surface Free Energy Determined with a Spectrophotometric Method. Environmental Science & Technology 49(10):6164-6171.

91. Park, B.-J., and N. I. Abu-Lail. 2011. The role of the pH conditions of growth on the bioadhesion of individual and lawns of pathogenic Listeria monocytogenes cells. Journal of colloid and interface science 358(2):611-620.

92. Sandre, O., L. Moreaux, and F. Brochard-Wyart. 1999. Dynamics of transient pores in stretched vesicles. Proceedings of the National Academy of Sciences 96(19):10591.

93. Olivi, M., E. Zanni, G. De Bellis, C. Talora, M. S. Sarto, C. Palleschi, E. Flahaut, M. Monthioux, S. Rapino, D. Uccelletti, and S. Fiorito. 2013. Inhibition of microbial growth by carbon nanotube networks. Nanoscale 5(19):9023-9029. 10.1039/C3NR02091F.

94. Hartono, M. R., A. Kushmaro, X. Chen, and R. S. Marks. 2018. Probing the toxicity mechanism of multiwalled carbon nanotubes on bacteria. Environmental Science and Pollution Research 25(5):5003-5012.

95. Lacerda, L., H. Ali-Boucetta, S. Kraszewski, M. Tarek, M. Prato, C. Ramseyer, K. Kostarelos, and A. Bianco. 2013. How do functionalized carbon nanotubes land on, bind to and pierce through model and plasma membranes. Nanoscale 5(21):10242-10250. 10.1039/C3NR03184E.

96. Linklater, D. P., H. K. D. Nguyen, C. M. Bhadra, S. Juodkazis, and E. P. Ivanova. 2017. Influence of nanoscale topology on bactericidal efficiency of black silicon surfaces. Nanotechnology 28(24):245301.

97. Dhahri, S., M. Ramonda, and C. Marlière. 2013. In-Situ Determination of the Mechanical Properties of Gliding or Non-Motile Bacteria by Atomic Force Microscopy under Physiological Conditions without Immobilization. PLOS ONE 8(4):e61663.

98. Modaresifar, K., L. B. Kunkels, M. Ganjian, N. Tümer, C. W. Hagen, L. G. Otten, P.-L. Hagedoorn, L. Angeloni, M. K. Ghatkesar, and L. E. J. N. Fratila-Apachitei. 2020. Deciphering the Roles of Interspace and Controlled Disorder in the Bactericidal Properties of Nanopatterns against Staphylococcus aureus. 10(2):347.

99. Bhattacharjee, S., C.-H. Ko, and M. Elimelech. 1998. DLVO Interaction between Rough Surfaces. Langmuir 14(12):3365-3375.

100. Linklater, D. P., S. Juodkazis, S. Rubanov, and E. P. Ivanova. 2017. Comment on “Bactericidal Effects of Natural Nanotopography of Dragonfly Wing on Escherichia coli”. ACS Applied Materials & Interfaces 9(35):29387-29393.

Figure Legends and Tables

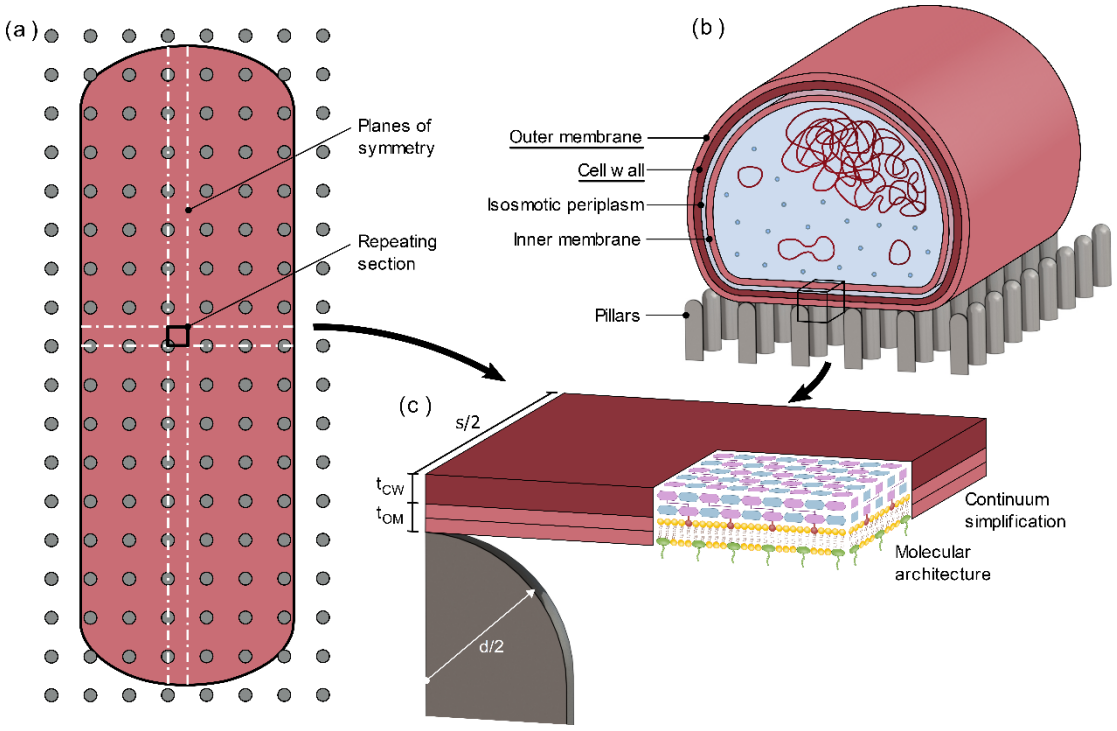

Figure 1. Reducing the bacteria-nanopattern problem. (a) Accurately scaled top view of a typically sized (1× 3μm) rod shaped bacteria on a nanopattern (*d* = 60nm, *s* = 180nm). (b) Central cross-section of a Gram-negative bacteria. Load bearing components are underlined. (c) Representative section used to model the bacteria-nanopattern problem with continuum smearing of molecular architecture.

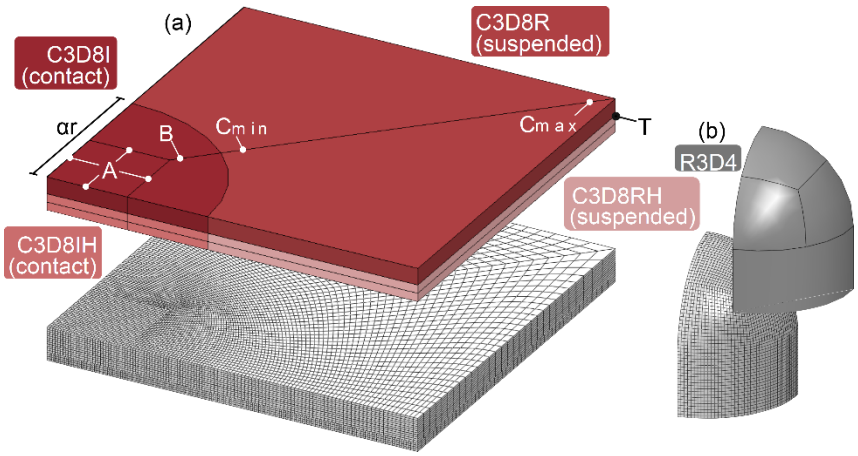

Figure 2. Element selection and mesh generation. (a) Envelope components are partitioned to enable use of mesh refinement and bending-specific elements in contact regions. (b) Partitioning of pillar to create smooth spherical mesh with hex elements.

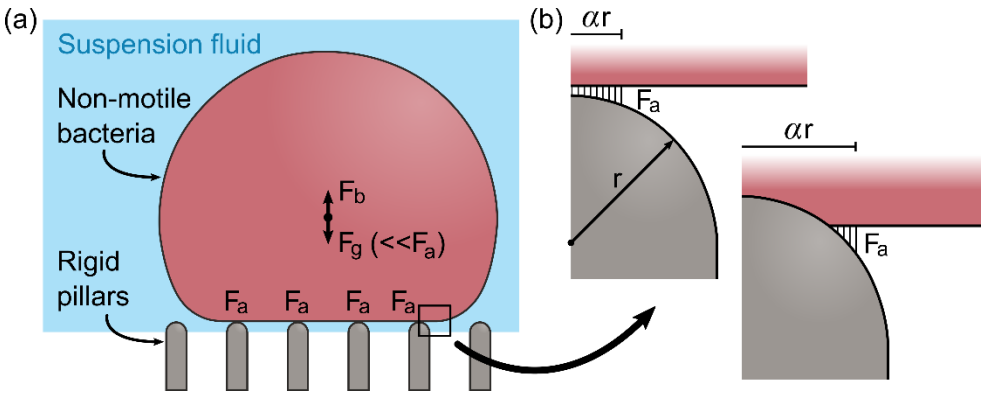

Figure 3. Free body diagram of an idealised, non-flagellated bacteria atop an array of rigid nanopillars. (a) The only significant force driving contact is from adhesion (F_a), whilst other physical forces such as weight (F_g) and buoyancy (F_b) are comparatively insignificant ($F_a >> F_g \sim F_b$). (b) Propagating bond front of finite ranged intermolecular adhesion forces.

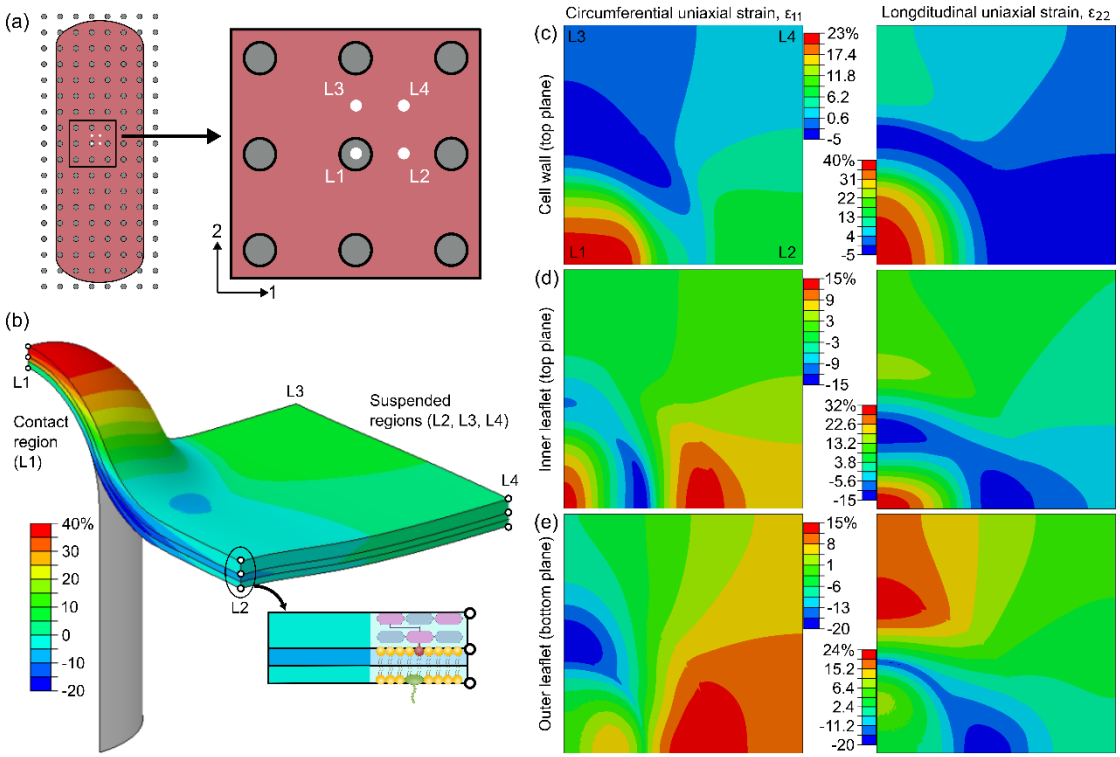

Figure 4. Probe locations to monitor the nonuniform deformation of the envelope. (a) Top view of the four locations which include the pillar apex (L1), the circumferential and longitudinal midpoints between two nearest pillars (L2 and L3), and the midpoint between an array of pillars (L4). (b) Contour plot of longitudinal uniaxial strain (ε_{22}) for an adhered envelope. Probe locations are shown and categorised into contact (L1) and suspended regions (L2, L3, L4). At each location, in-plane uniaxial strains are probed at three points through the thickness, representing each of the three layers. For the inner and outer leaflets, the points correspond to the position of hydrophilic head groups (top and bottom planes, respectively). For the cell wall, the maximum through-thickness value is probed, which is found at the top plane. (c-e) Contours plots of circumferential (ε_{11}) and longitudinal (ε_{22}) uniaxial strain for each envelope layer. All contour plots are for the soft envelope configuration with an adhesion energy, dimensionless sinking depth, pillar diameter and centre-to-centre spacing of 21mJ/m^2, 1.36, 60nm and 180nm, respectively.

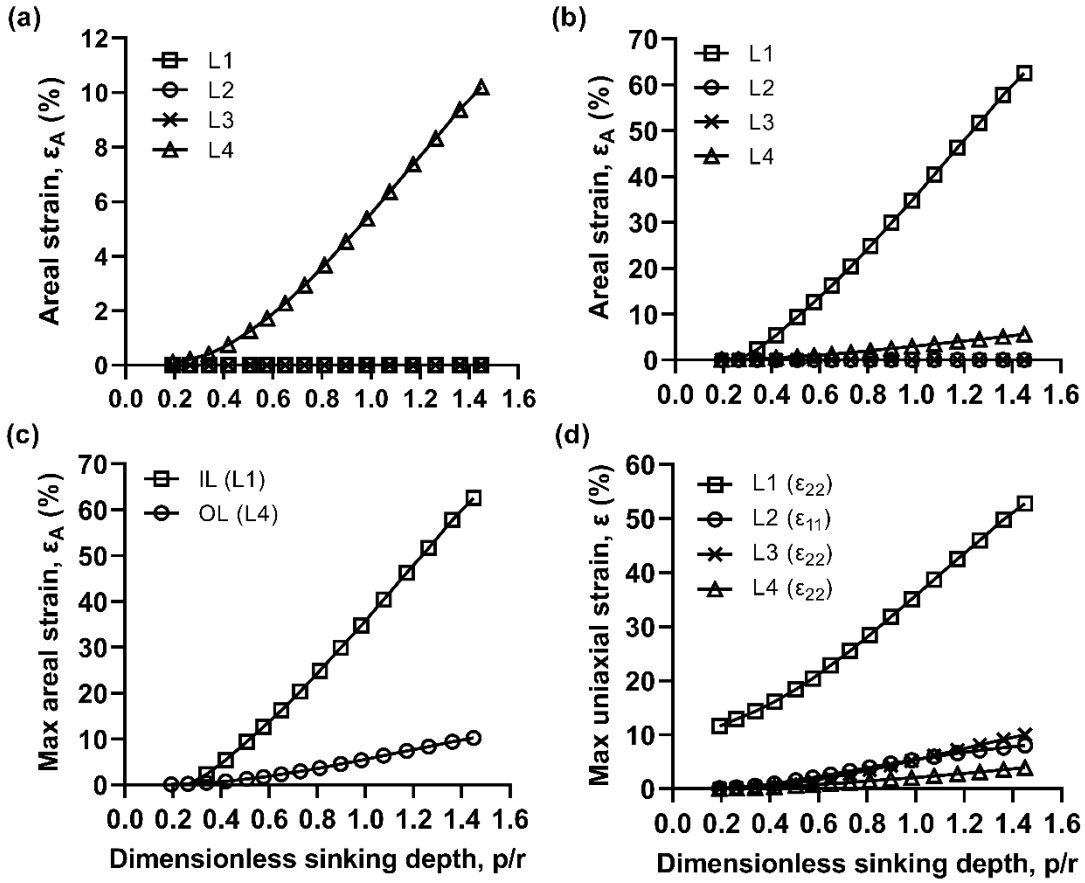

Figure 5. Evolution of in-plane tensile strains with dimensionless sinking depth (*p/r*) at contact (L1) and suspended (L2, L3, L4) regions. (a) Areal strains within the outer leaflet. (b) Areal strains within the inner leaflet. (c) Comparison of maximum areal strains in the inner (IL) and outer (OL) leaflets of the bilayer membrane. (d) Maximum uniaxial strain in the cell wall. Data is for the soft envelope configuration with a pillar diameter and pattern spacing of 60nm and 180nm, respectively.

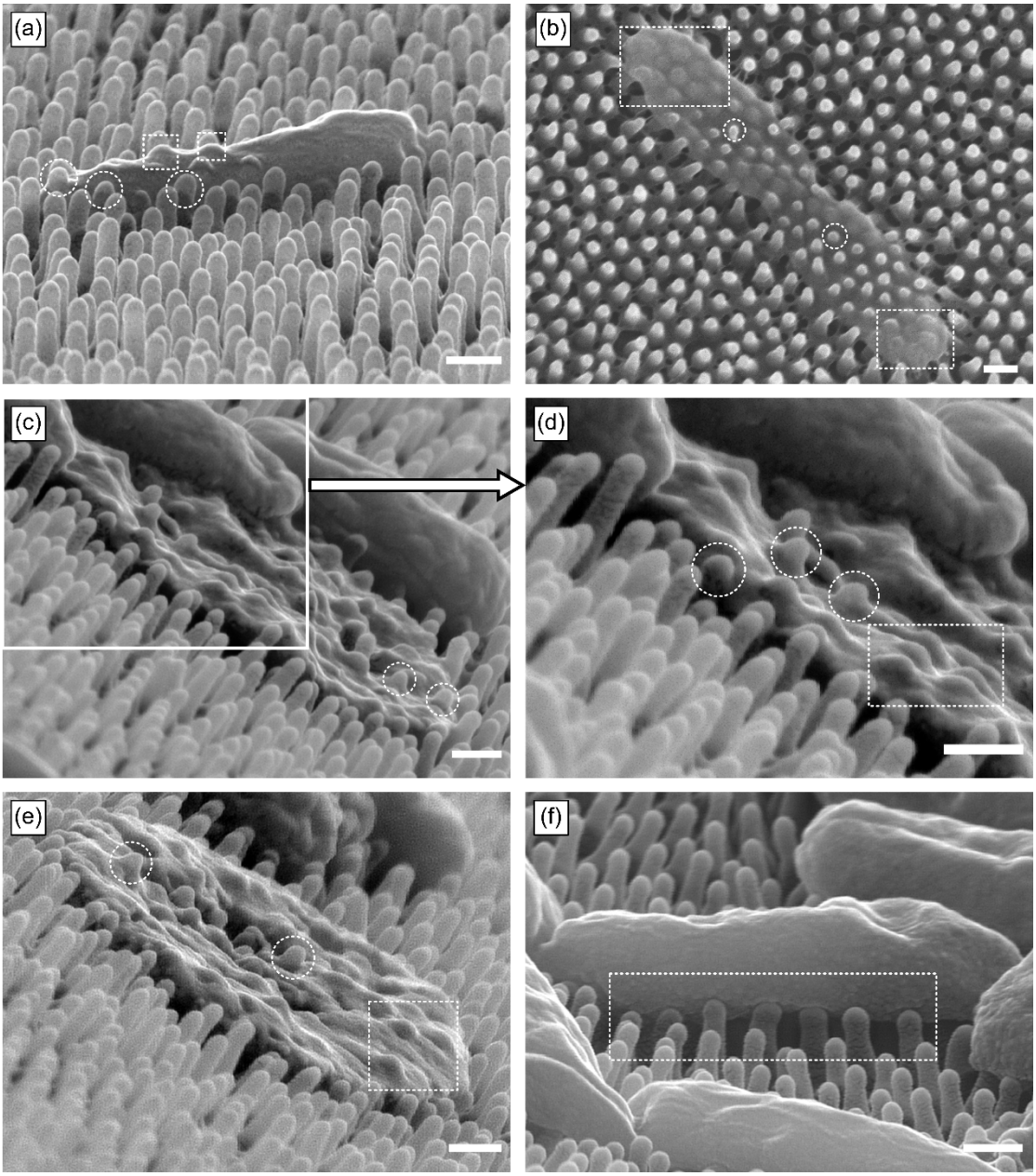

Figure 6. Gram-negative *Pseudemonas aeruginosa* adhered to the wing nanopattern of the *Psaltoda claripennis* cicada. (a) Penetrated cell retaining some shape and turgor. (b-e) Penetrated cells with total loss of turgor. (f) Cells with some turgor loss, but no clear signs of penetration, only perturbation. Circular and rectangular outlines are used to highlight penetration and perturbation, respectively. Scale bars are 200nm.

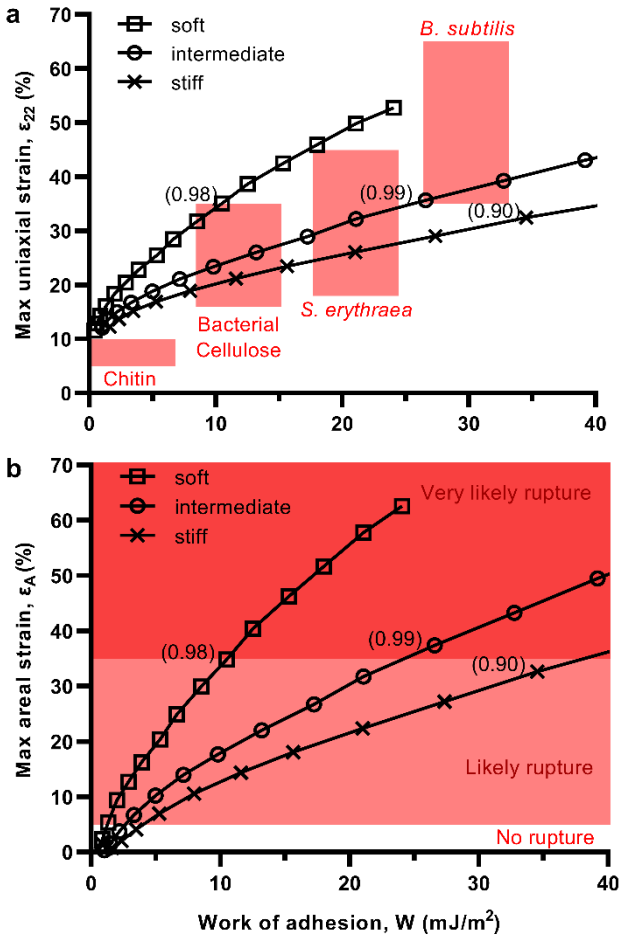

Figure 7. Work of adhesion required to deform Gram-negative bacteria. (a) Assessment of cell wall deformation by maximum uniaxial strain in longitudinal direction (ε_{22}), probed at pillar apex. (b) Assessment of outer membrane deformation by maximum areal strain (ε_A), probed at pillar apex. Bracketed values indicate corresponding dimensionless sinking depth (p/r). Data is for pillar diameter and pattern spacing of 60nm and 180nm, respectively.

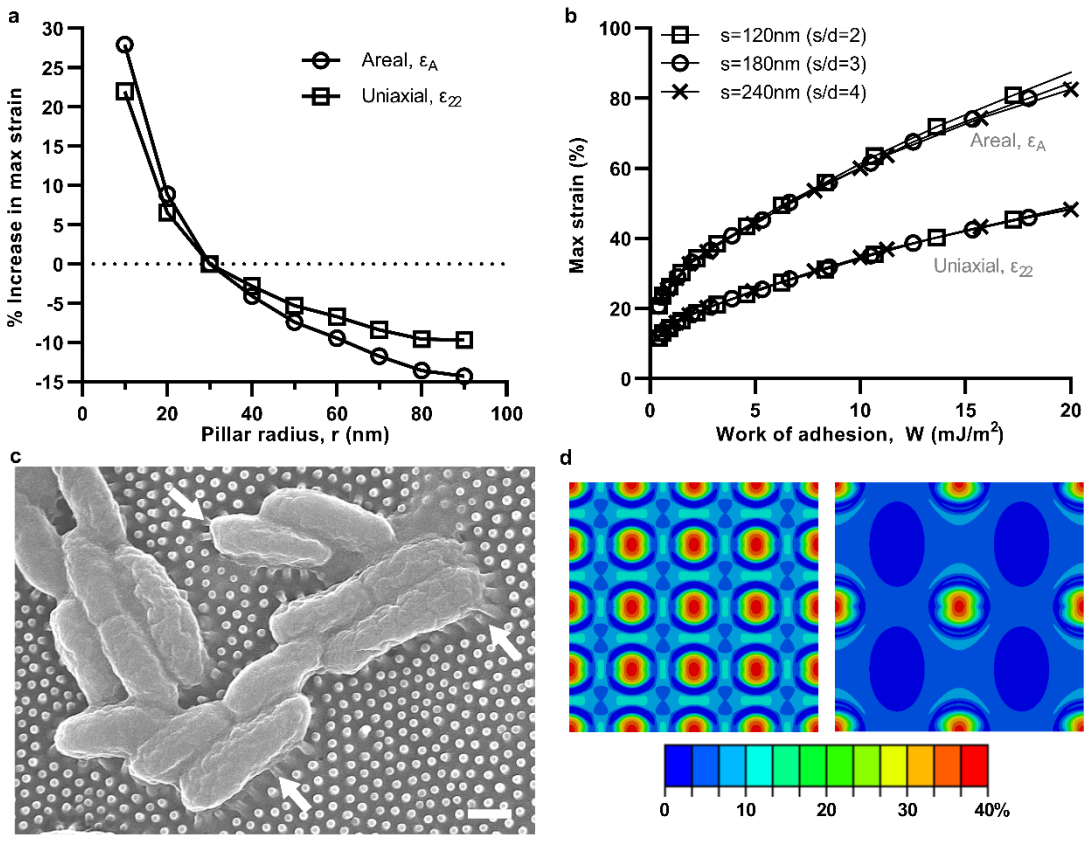

Figure 8. Impact of individual geometric parameters. (a) Percentage increase in maximum uniaxial and areal strain due to pillar radius at an adhesion energy, dimensionless spacing and pillar height of 10mJ/m^2, 3 and 200nm, respectively. (b) Effect of dimensionless spacing on maximum areal and uniaxial strain at a pillar radius and height of 30nm and 200nm, respectively. (c) Bending of cicada wing pillars at the periphery *P. aeruginosa* cells, highlighted with arrows. Scale bar is 500nm (d) Top-view contour plots of maximum uniaxial strain for spacing of 120nm (left) and 240nm (right) at an adhesion energy, pillar radius and pillar height of 20mJ/m^2, 30nm and 200nm, respectively. All data shown is for the soft envelope configuration.

Table 1. Constitutive models for Gram-negative envelope

Part	Material model	Parameter	Selection			Estimate	Ref.
			Soft	Intermediate	Stiff		
Outer membrane	Isotropic neo-Hookean	C_{10}	1.61 MPa	4.83 MPa	8.05 MPa	K_A = 50 – 250mN/m	(33, 41-43) (44)
		D_1	0.018 MPa^{-1}	0.006 MPa^{-1}	0.004 MPa^{-1}	v_{OM} = 0.485	
		t_{OM}	4nm (2nm per leaflet)			3-5nm	(43, 45)
Cell wall	Orthotropic elastic	E_1 (=E_G)	25 MPa	50 MPa	75 MPa	25 – 75MPa	(46-48)
		E_2, E_3 (=E_P)	10 MPa	20 MPa	30 MPa	10 – 30MPa	(48-50)
		v_{12}, v_{13}, v_{23}, v_{32} (=v_{GP})	0.35			0.32 – 0.67	(47, 51)
		v_{21}, v_{31} (=v_{PG})	0.14			0.01 – 0.23	(47, 51)
		G_{12}, G_{13} (=G_{GP})	5.3 MPa	10.5 MPa	15.8 MPa	3.55 – 17.95 MPa	(Supporting Material A)
		G_{23} (=G_P)	3.7 MPa	7.4 MPa	11.1 MPa	3.7 – 11.1 MPa	
		t_{CW}	4nm			2-6nm	(46, 50, 52)

Table 2. interactions involved in the adhesion of a bacterial envelope to a nanopattern

Interaction	Contact surface		Type	Constraint method	Contact properties	
	Master	Slave			Normal	Tangential
Surface adhesion	Pillar	Outer leaflet	Surface-to-surface contact	Penalty and finite sliding	Hard (no separation)	Rough ($\mu=\infty$)
Hydrophobic effect	Outer leaflet	Inner leaflet	Surface-to-surface contact	Penalty and finite sliding	Hard (no separation)	Frictionless ($\mu=0$)
Lipoprotein linkage	Inner leaflet	Cell wall	Tie constraint	Surface-to-surface discretization	No relative motion	